



Multicomponent material property characterization of atherosclerotic human carotid arteries through a Bayesian Optimization based inverse finite element approach[☆]

Su Guvenir Torun^{a,*}, Hakki M. Torun^b, Hendrik H.G. Hansen^c, Chris L. de Korte^c, Antonius F. W. van der Steen^a, Frank J.H. Gijsen^{a,d}, Ali C. Akyildiz^{a,d}

^a Department of Biomedical Engineering, Erasmus Medical Center, 3015 GD, Rotterdam, the Netherlands

^b School of Electrical and Computer Engineering, Georgia Institute of Technology, Atlanta, GA, USA

^c Department of Medical Imaging, Radboud University Medical Center, Nijmegen, the Netherlands

^d Department of Biomechanical Engineering, Delft University of Technology, the Netherlands

ARTICLE INFO

Keywords:

Atherosclerosis
Bayesian
Carotid
Finite element
Inflation
Material constant
Plaque rupture
Yeoh

ABSTRACT

Objective: Plaque rupture in atherosclerotic carotid arteries is a main cause of ischemic stroke and it is correlated with high plaque stresses. Hence, analyzing stress patterns is essential for plaque specific rupture risk assessment. However, the critical information of the multicomponent material properties of atherosclerotic carotid arteries is still lacking greatly. This work aims to characterize component-wise material properties of atherosclerotic human carotid arteries under (almost) physiological loading conditions.

Methods: An inverse finite element modeling (iFEM) framework was developed to characterize fibrous intima and vessel wall material properties of 13 cross sections from five carotids. The novel pipeline comprised ex-vivo inflation testing, pre-clinical high frequency ultrasound for deriving plaque deformations, pre-clinical high-magnetic field magnetic resonance imaging, finite element modeling, and a sample efficient machine learning based Bayesian Optimization.

Results: The nonlinear Yeoh constants for the fibrous intima and wall layers were successfully obtained. The optimization scheme of the iFEM reached the global minimum with a mean error of 3.8% in 133 iterations on average. The uniqueness of the results were confirmed with the inverted Gaussian Process (GP) model trained during the iFEM protocol.

Conclusion: The developed iFEM approach combined with the inverted GP model successfully predicted component-wise material properties of intact atherosclerotic human carotids ex-vivo under physiological-like loading conditions.

Significance: We developed a novel iFEM framework for the nonlinear, component-wise material characterization of atherosclerotic arteries and utilized it to obtain human atherosclerotic carotid material properties. The developed iFEM framework has great potential to be advanced for patient-specific in-vivo application.

1. Introduction

Stroke is amongst the leading causes of death worldwide, and twelve million people are estimated to have stroke-related mortality globally in the upcoming decade (Feigin et al., 2014). Approximately 90% of the clinical cases develop in the form of ischemic stroke (Mozaffarian et al., 2016), and an important cause of ischemic stroke is the rupture of

atherosclerotic plaques in carotid arteries (Chunet et al., 2002). Currently, the standard preventive surgical treatment of carotid atherosclerosis is the removal of the plaque from the artery, referred to as endarterectomy procedure. However, only a very limited proportion of patients (~20%) was shown to benefit from this surgery (Rothwell and Warlow, 1999). A major reason for this poor outcome is considered to be the sub-optimal assessment of the carotid atherosclerosis severity, which is mainly based

[☆] This work was supported in part by the European Commission's Horizon 2020 research and innovation programme under the Marie Skłodowska-Curie grant agreement # 749283.

* Corresponding author.

E-mail address: s.guvenir@erasmusmc.nl (S. Guvenir Torun).

<https://doi.org/10.1016/j.jmbbm.2021.104996>

Received 15 May 2021; Received in revised form 1 November 2021; Accepted 23 November 2021

Available online 27 November 2021

1751-6161/© 2021 The Authors.

Published by Elsevier Ltd.

This is an open access article under the CC BY-NC-ND license

(<http://creativecommons.org/licenses/by-nc-nd/4.0/>).

on the stenosis degree of the atherosclerotic carotid artery. Stenosis degree provides a measure for the blood flow through the artery; however, does not reflect the plaque rupture risk (Tavora et al., 2010). Hence, there is an urgent need for plaque rupture risk assessment tools to achieve better clinical outcome.

From the mechanical viewpoint, plaque rupture is the material failure of the plaque tissue, which was shown to associate with blood pressure-driven, intraplaque structural stresses (Cheng et al., 1993), (Richardson, 1989). Hence, biomechanical evaluations that include intraplaque stress analyses hold a great potential to aid plaque rupture risk assessment (Holzapfel et al., 2014). Intraplaque stresses are commonly evaluated by means of finite element (FE) analysis (Cheng et al., 1993; Richardson, 1989; Holzapfel et al., 2014; Loree et al., 1992; Akyildiz et al., 2011; Sadat et al., 2011). The great impact of the structural composition and resulting geometry of the multi-component atherosclerotic artery structure, with the main mechanically relevant plaque components being fibrous intima, lipid pool, calcium, media and the adventitia, on the intraplaque stresses have been demonstrated before (Akyildiz et al., 2011, 2016a, 2018). Another essential requirement for accurate stress computations with FE plaque models is the correct and precise material behavior information of the heterogeneous atherosclerotic artery (Akyildiz et al., 2011).

It has been previously demonstrated that the atherosclerotic plaques, even the ones from the same vascular territory, may show great variance in material properties (Akyildiz et al., 2014). Therefore, one would ideally prefer plaque-specific material characterization from *in-vivo* measurements for stress analysis, especially to aid plaque-specific rupture risk assessment. Unfortunately, there is no well-established approach currently available that would serve this purpose. Our existing knowledge on plaque properties is based on *ex-vivo* experimental work, that involve bench-top tensile (Learoyd and Taylor, 1966; Teng et al., 2009; Maher et al., 2009; Lawlor et al., 2011; Mulvihill and Walsh, 2013; Tenget al., 2014; Kural et al., 2012; Davis et al., 2016; Cunnane et al., 2016; Wanget al., 2019; O'Reilly et al., 2020) and compression tests (Maher et al., 2009), (O'Reilly et al., 2020; Chai et al., 2013; Chai et al., 2014; Chai et al., 2015; Barrett et al., 2009; Ebenstein et al., 2009; Maher et al., 2011; Heiland et al., 2013). A comprehensive summary could also be found elsewhere (Teng et al., 2014). However, the results of these studies are limited to average plaque tissue properties as the tests were usually performed on entire plaque or artery sections, and the test data was analyzed assuming tissue homogeneity. Although the great previous work deepened our understanding in overall biomechanical response of the plaque tissue, it does not provide the essential component-wise information of the highly heterogeneous atherosclerotic carotid arteries. Some recent work (Tenget al., 2014), (Wanget al., 2019) has overcome this limitation by performing mechanical tests on individual plaque components and clearly demonstrated the need for component-wise material characterization of atherosclerotic plaques. However, the tensile tests employed in these studies do not reflect the multi-axial physiological loading the arteries are exposed to *in-vivo*. In addition, the preparation of test samples for the tensile tests lead to loss of tissue's structural integrity, which may result in inaccurate material property estimation.

Ex-vivo inflation tests can overcome the abovementioned limitations by closely mimicking the physiological loading conditions and enabling intact atherosclerotic artery testing. Previously Boekhoven et al. performed inflation tests to carotid plaques (Boekhoven et al., 2016) but the authors could reach only sub-physiological pressures in the tests as they tested endarterectomy samples separated from the surrounding media-adventitia complex (i.e arterial wall). Recently our group developed a hybrid experimental-numerical approach, an inverse FE modeling (iFEM) approach, to extract component-based material properties of atherosclerotic arteries from intact vessel inflation experiments and tested its feasibility with atherosclerotic porcine iliac arteries (Akyildiz et al., 2016b). This approach combined inflation testing of intact vessels, ultrasound-derived plaque deformation measurements and

histology-derived plaque morphology assessment.

In the current study, we further advance our approach in multiple aspects and extract multicomponent properties of atherosclerotic human carotid arteries, for the first time, under physiological-like loading conditions. The advancements include high-resolution magnetic resonance imaging (MRI) for plaque morphology, employing nonlinear hyperelastic material models for plaque components and use of a sample-efficient machine-learning based optimization algorithm combined with uniqueness approximation, which all together bring our approach closer to clinical use for patient-specific material characterization.

2. Materials and methods

The developed iFEM approach consists of three main parts: 1. *ex-vivo* inflation testing combined with a high-frequency ultrasound system to obtain deformation, 2. high-resolution pre-clinical MRI derived FE modeling, and 3. sample efficient Deep Partitioning Tree based Bayesian Optimization (DPTBO) (Fig. 1). In addition, the uniqueness of the iFEM predicted properties were evaluated. All parts are explained below.

2.1. Ex-Vivo inflation testing

2.1.1. Sample preparation

Atherosclerotic carotid arteries from five human cadavers (population age >40 years) were collected within the last 2 years before the mechanical testing in Erasmus Medical Center in Rotterdam, the Netherlands. The sample collection was approved by the Medical Ethical Committee of Erasmus Medical Center regarding the Helsinki Declaration. The intact carotids were snap frozen with liquid nitrogen after collection and stored at -80°C until mechanical testing. The storage at -80°C is expected to preserve the mechanical properties of the tissues (Schaar et al., 2002). On the day of the inflation tests, the tissues were thawed at room temperature. Then, the perivascular tissue surrounding the carotids was removed. The arteries were kept immersed in a Phosphate Buffered Saline (PBS) solution to prevent dehydration during the preparation. The external branch of the carotid arteries were suture fixed, to prevent leakage during the inflation. Male luer slips were glued and suture-fixed to the common and the internal branch ends of the arteries (Fig. 2).

2.1.2. Inflation tests and high frequency ultrasound imaging

Following the tissue preparation, the intact carotids were placed into the custom built inflation test setup. In the setup, the atherosclerotic human carotid arteries were placed inside a tissue bath filled with 37°C PBS solution (Fig. 2). Longitudinal stretching of the arteries could be adjusted within the setup by using the pipette with longitudinal direction motion capability. Pressure was applied by using a syringe pump, and a digital manometer (accuracy of 1.7 mmHg) (2022P, Digitron) was used for the pressure measurements. Prior to the mechanical testing, the arteries were preconditioned by applying 10 cycles of 15% longitudinal stretch and 10 cycles of intraluminal pressurization up to 120 mmHg. The inflation tests were performed while the arteries were kept at 15% longitudinal pre-stretch which was reported as the in-situ pre-stretch level for the carotid arteries of the people that match the age group of our sample set (Horný et al., 2017).

During *ex-vivo* inflation tests, quasi-static pressure steps were applied in 10 mmHg increments up to 120 mmHg, with no signs of buckling in the arteries. At each pressure step, the arteries were scanned with a pre-clinical ultrasound system (Vevo 2100, FUJIFILM Visual Sonics Inc., Toronto, Canada) by using a high frequency, 2-D linear transducer (MS250, 21 MHz central frequency). The transducer was connected to the 3-D motor stage of the ultrasound system, which moved the transducer along the artery's longitudinal direction and acquired 2-D ultrasound data at every 0.24 mm. Before each inflation experiment, an ultrasound pre-scan of the artery was performed to identify the location of the plaque region in the artery. During the inflation tests, B-

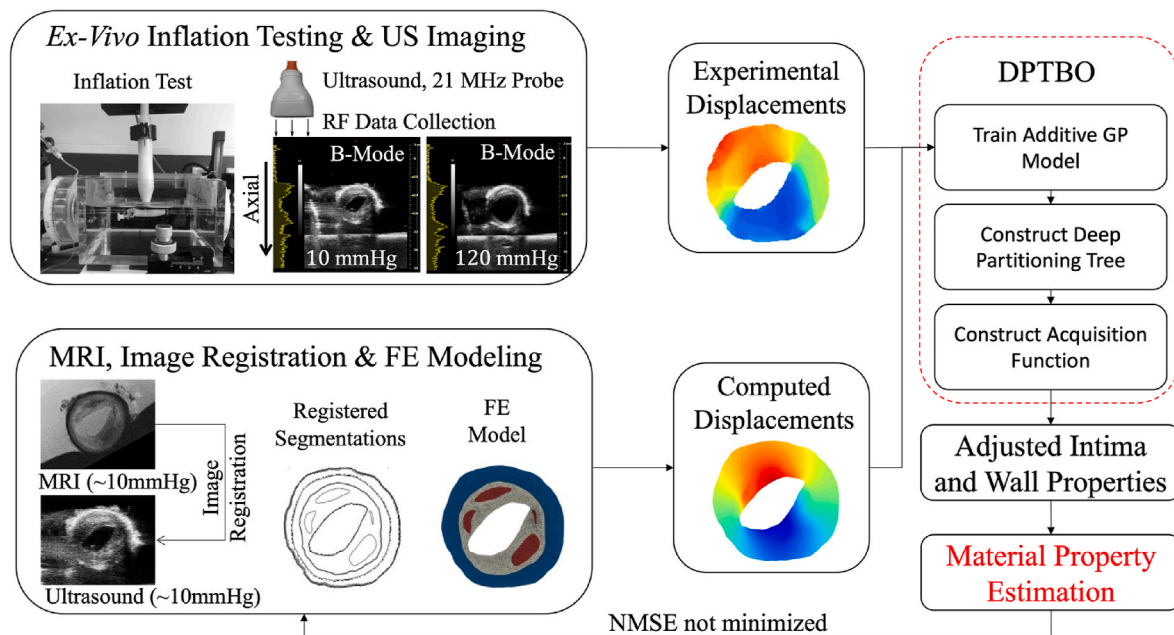


Fig. 1. iFEM pipeline comprising of three main parts, namely the ex-vivo inflation testing combined with ultrasound imaging, MRI geometry based FE modeling and the DPTBO.

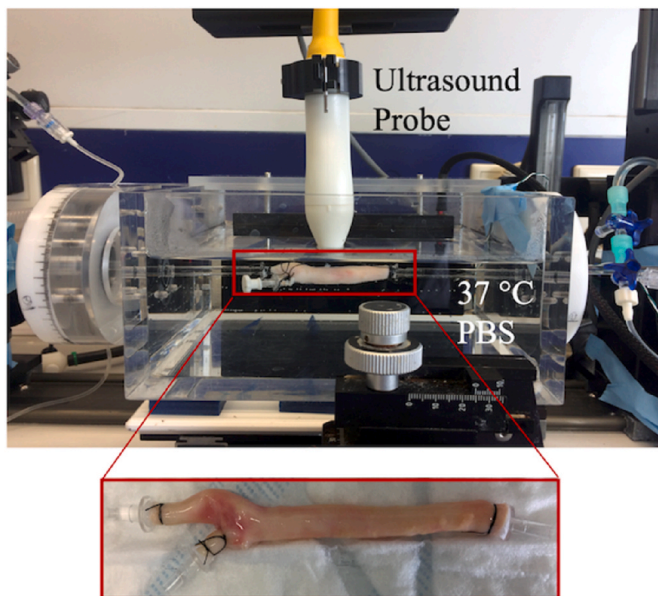


Fig. 2. The custom built inflation setup to test atherosclerotic human carotid arteries, and the 21 MHz ultrasound probe.

mode images and radiofrequency (RF) data were collected at multiple cross sections of each artery. Example ultrasound images of an atherosclerotic carotid cross section at a low (10 mmHg) and a high (120 mmHg) pressure are demonstrated in Fig. 3.

The acquired RF data were used to accurately estimate the full-field deformation of the inflated heterogeneous atherosclerotic plaques, by using a coarse-to-fine normalized cross-correlation-based algorithm (Lopata et al., 2009). Briefly, this algorithm estimates the full-field displacement of the arterial cross sections in three iterative steps by spatial templates of ultrasound data at one pressure step within a larger search region using data of a subsequent step. As matching criterion the value of the normalized cross-correlation function is used. The position of the peak of this function gives a direct estimate of the displacement at

the center of each template that occurred between the considered pressure steps. The analysis begins in iteration 1 and 2 with a coarse estimation of the 2-D displacement field based on the envelope of the RF data and ends in iteration 3 with a fine estimation using smaller kernels and subsample motion estimation based on RF data. The found displacements of previous iterations were used as offset for the search kernels in successive iterations to guide the algorithm to the best match on a fine level. In iteration 1, the template and search kernel size were 978 (axial) by 675 (lateral) μm^2 and 3422 by 1575 μm^2 with a spacing of 978 μm axially and 45 μm laterally between the centers of templates. In iteration 2, the template and search kernel sizes were reduced into 489 (axial) x 405 (lateral) μm^2 and 733 (axial) x 855 (lateral) μm^2 , respectively. The axial spacing between the centers of templates was decreased to 55 μm while the lateral spacing remained 45 μm . Then, for the last iteration, kernel and template sizes were reduced to 244 by 225 μm^2 and 293 by 315 μm^2 . The spacing between template centers remained the same as in iteration 2. In this iteration, the raw RF data instead of its envelope were matched, and the cross-correlation peak was interpolated using bicubic interpolation to obtain the 2-D displacement at subsample level, thus smaller than the sample distance of the RF data which was 6 by 45 μm^2 . Full-field displacement measurements of the arterial transversal cross section under increasing intraluminal pressurization were obtained at the end of the iterations with 55 (axial) x 45 (lateral) μm^2 resolution. Please note that the axial and lateral directions refer to 2-D cross sectional ultrasound images. For further details of the approach, the reader is referred to the previous publications by Lopata et al. (2009) and Hansen et al. (2012).

2.2. FE modeling

2.2.1. Plaque morphology from high magnetic field MRI

To build accurate FE models, detailed morphological information was needed. Although the ultrasound images provide the information of the lumen border and the external elastic lamina (media/adventitia border), they do not provide the required information to delineate the structural components of atherosclerotic artery completely. The missing crucial geometric information of heterogeneous plaques were obtained from high in-plane resolution (50 μm x 50 μm), multisequence *ex-vivo* MRI, recorded by a high magnetic field (7 T) pre-clinical MR scanner

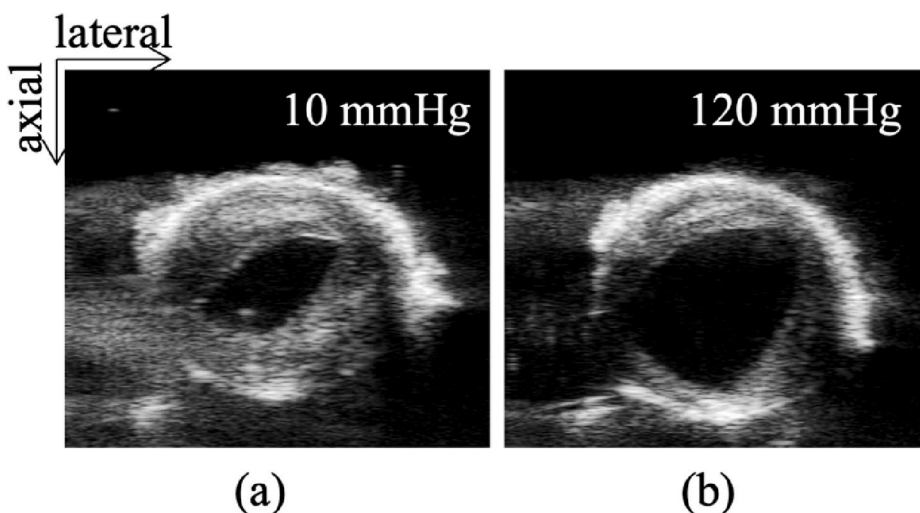


Fig. 3. B-mode ultrasound images of a carotid cross section for at 10 mmHg (a) and 120 mmHg (b) pressures.

(Discovery MR901, General Electric).

The MRI scans were performed while a very low intraluminal static pressure (10 mmHg) was applied to the arteries to prevent the collapse of the lumen during the scanning. In order to apply the intraluminal pressure, the arteries were connected to pipettes which were closed by three-way valves. From one end, the pressure was induced by a PBS filled syringe, and on the other end, a manometer was attached to measure the applied pressure. When the pressure was observed to be stabilized at approximately 10 mmHg, the three-way valves were locked, and the syringe and the manometer were detached from both ends. The arteries were scanned submerged in PBS to prevent any dehydration during the scanning. T1 and T2-weighted sequences were used and 512×512 pixels images were obtained from the MRI scans. The details of the MRI sequences were as follow: T1-weighted: flip angle = 20° , repetition time = 17.5 ms, echo time 3.3 ms; T2-weighted: flip angle = 90° , repetition time = 2500 ms, echo time 60 ms. The longitudinal slice thickness was 0.5 mm for both sequences.

2.2.2. Image segmentation and ultrasound-MRI co-registration

Following the previously described guidelines (Shinnaret al, 1999), (Serfaty et al., 2001), T1-and T2-weighted MR images (Fig. 4) were segmented for fibrous intima, lipid pool, calcifications and arterial wall morphologies by using ITK-Snap (Yushkevichet al, 2006) (Fig. 4). Both T1-and T2-weighted MR images clearly showed the lumen and the outer vessel border, due to the intensity difference between the arterial structure and the PBS. The calcified regions were identified by the hypo-intense signal in both T1-and T2-weighted images (Shinnaret al, 1999). The lipid pools were identified as the hypo-intense regions in T2-weighted images, with iso-intense or hyper-intense characteristics in T1-weighted images (Shinnaret al, 1999). Adventitia appeared as hypo-intense region, whereas media had a higher signal intensity (Serfaty et al., 2001).

To obtain a representative dataset, a subset of transversal plaque cross sections from the tested carotid arteries (2–3 per artery) were selected for the IFEM analysis. The inclusion assessment for the selected cross sections was based on the plaque size, the location, and the quality of MRI and ultrasound images. First, the cross sections from the internal

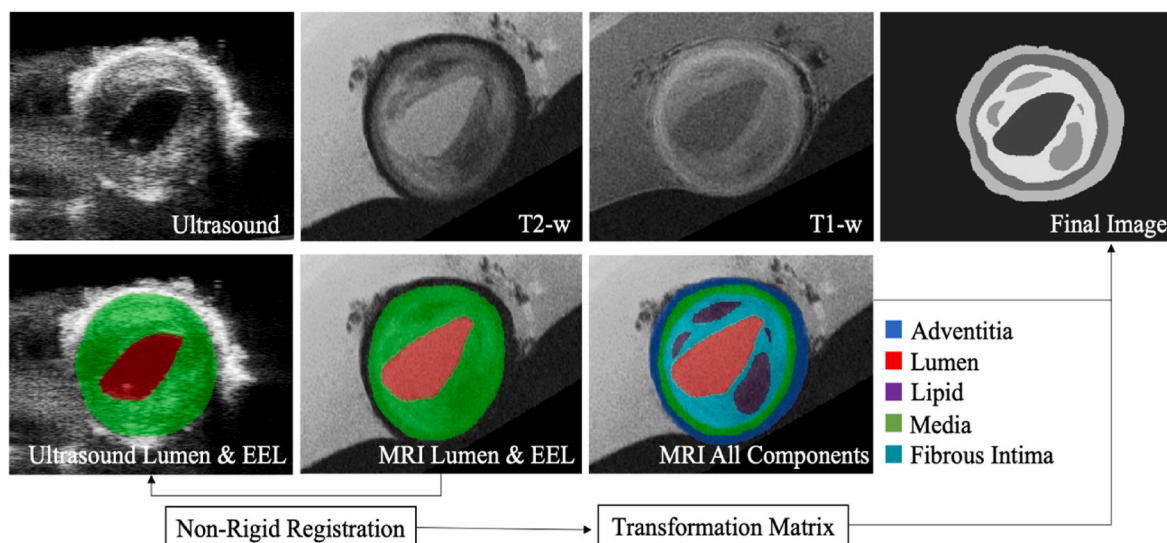


Fig. 4. Ultrasound and co-registered T1 and T2-weighted MR images of a sample with lipid pools. The lumen (red) and external elastic lamina (EEL) (green) were segmented both on the ultrasound and MR images to obtain the transformation matrix by the non-rigid registration. Then, the transformation matrix was applied on the lumen (red), fibrous intima (turquoise), lipid (purple), media (green) and the adventitia (blue) segmented T2-weighted MR image to obtain the final registered image.

and common carotid branches with the largest plaque area and minimum lumen area were selected. Then, extra cross sections were selected, by ensuring a minimum distance of 1.5 mm from each other. Cross sections were at least 5 mm away from the bifurcation. Furthermore, the cross sections had to have a clear image on MRI and ultrasound, free of artifacts. This procedure led to a selection of 13 cross sections from five carotid arteries tested.

An image registration step (Fig. 4) was necessary to transfer the information of each component obtained from MRI to the ultrasound images, since the experimental deformations were obtained by the ultrasound system. The reference ultrasound and MRI images at 10 mmHg were used for the registration. In the registration, the first step was to identify the longitudinal location of the selected cross sections. This was done by measuring the distance of the cross sections from natural morphological landmarks such as the bifurcation, and cannulas in both ultrasound and MR images. Then, a rigid registration was performed by using the custom-built plug-in at the Mevis-Lab Software (Version 2.7) (MeVis Medical Solutions AG, Fraunhofer Institute for Digital Medicine MEVIS) to adjust the spatial resolution of the MRI to the ultrasound. Afterwards, the lumen and external elastic lamina borders were segmented on the ultrasound and the co-registered MR images by using ITK-Snap (Yushkevich et al., 2006) (Fig. 4). These segmentations were used in *elastix* software (Version 5.0) (Klein et al., 2010), (Shamonin et al., 2014) to obtain a transformation matrix to register the MR images to the ultrasound images. Then, the fibrous intima, media, adventitia, lipid and calcifications on the MR images were manually segmented and non-rigid registration was performed by applying the transformation matrix obtained with *elastix*. After the rigid and non-rigid registrations, the final registered segmentations with the component-wise morphological information was obtained (Fig. 4).

2.2.3. FE modeling and plaque deformation computations

The final registered segmentations were used to create 2-D FE models of the selected cross sections ($n = 13$). The models were used to simulate the deformation of the atherosclerotic carotid arteries during inflation testing. The composition of the atherosclerotic arteries were reflected in the FE models by a multicomponent arterial structure that consisted of fibrous intima, arterial wall (comprising media and adventitia), lipid pools, and calcifications. The FE models were created and simulated by using ABAQUS (Dassault Systèmes, 2016). The fibrous intima and the arterial wall were modeled as isotropic, nonlinear, hyperelastic, incompressible Yeoh solids, described with the strain energy density function, W_{Yeoh} , as

$$W_{\text{Yeoh}} = \sum_{i=1}^3 c_i (I_1 - 3)^i \quad (1)$$

where c_i are the material constants and I_1 is the first invariant of the right Cauchy-Green deformation tensor. The calcifications and lipid pools were modeled as Neo-Hookean solids, with a strain energy density function, W_{NH} , given as

$$W_{\text{NH}} = c_1 (I_1 - 3) \quad (2)$$

where c_1 is the material constant. The calcifications were defined as highly stiff, incompressible materials with c_1 of 1 GPa, and the lipid pools were defined as highly compliant, incompressible materials with a c_1 value of 1 kPa. A highly compressible and compliant buffer of a Neo-Hookean solid (c_1 of 0.1 kPa) encompassed the arterial cross sections in the FE models to minimize rigid body motion and enforce simulation convergence. Hybrid formulation triangular and quadrilateral elements were used for meshing the FE models. Following a mesh convergence analysis, FE models were meshed with 48k (± 5 k) elements on average (\pm SD). The simulations were performed under plane strain assumption. The computational deformation results from the pressure steps of 80, 100 and 120 mmHg were used in the optimization. The axial

displacement data were obtained as the measure of deformation as the final output of FE simulations.

2.3. Optimization process for material property assesment

A grid with an element size of $100 \times 100 \mu\text{m}^2$ was applied on the arterial cross sections. Measured and computed axial displacements per grid element were calculated by averaging displacements from ultrasound and FEM computations, respectively. Then, the relative displacements (measured and computed) were obtained by using the top central grid element as reference. The normalized mean square error (NMSE) between the experimental and the computed relative displacements was calculated and by the DPTBO in an iterative manner. At each iteration the Yeoh model material constants of the fibrous intima and arterial wall components in the FEM were revised and a new simulation was performed with a new set of material constant values. The NMSE (Torun and Swaminathan, 2019) is calculated according to (3), where N is total number of grid elements, $y(x)$ is the experimentally obtained displacements and $\hat{y}(x)$ is the FE model predicted displacements.

$$f(x) = \text{NMSE} = \frac{\sum_{i=1}^N (\hat{y}(x_i) - y(x_i))^2}{\sum_{i=1}^N \left(y(x_i) - \frac{1}{N} \sum_{i=1}^N y(x_i) \right)^2} \quad (3)$$

For the NMSE evaluation in the optimization scheme, only the data from the central region (50% of the width of the cross sections) was used.

The optimization problem posed by the iFEM framework corresponds to finding the global minimum of a possibly non-convex function, defined as

$$\bar{x} = \arg\min_{x \in \mathcal{X}} f(x) \quad (4)$$

where x is the D-dimensional input vector, $\mathcal{X} \in \mathcal{R}^D$ is the optimization search space and $f(\cdot) : \mathcal{X} \rightarrow \mathcal{R}$ is the objective function to be minimized. In the iFEM framework, x in (4) corresponds to the material constants of the Yeoh models of the fibrous intima and arterial wall components and $f(\cdot)$ is defined as the error, more specifically NMSE, between experimentally obtained and FE model predicted axial displacements as in (3). The optimization stopped after 400 iterations.

A major challenge of the optimization problem in hand is the objective function queries corresponding to computationally intensive FE simulations as increasing number of function evaluations can lead to impractical computational requirements. Hence, the goal of the optimization algorithm used in the iFEM framework is to find the optimum material properties that minimize the objective function, $f(\cdot)$, using as few function evaluations as possible. However, conventional techniques, such as gradient-based and evolutionary ones, often times show poor performance in such optimization problems (Swaminathan et al., 2020).

To address these optimization related challenges, we employed a machine learning based global optimization technique, namely Bayesian Optimization (BO). BO is a class of active learning based machine learning method and specially aims to minimize number of function evaluations required to find the global minimum of non-convex and black-box functions. Hence, it is a very promising alternative to conventional algorithms for material property estimation purposes through iFEM. BO combines two components to solve the optimization problem in (4), namely a probabilistic model and a sampling strategy. More specifically, at t^{th} iteration of the optimization, previously collected function queries, $\{x_i, f(x_i)\}_{i=1}^t$, are used to train a Gaussian Process (GP) model. The role of GP is to approximate the objective function, $f(\cdot)$, and provide a predictive posterior distribution to estimate the value of function at non-queried input locations. The GP posterior is then used to create the sampling strategy called as an acquisition function, $u(x)$. The acquisition function is then maximized using an auxiliary optimization procedure and the resulting point is selected as the next sampling point

(x_{t+1}), i.e. next material constant combination to be used in the optimization loop. It should be noted that the auxiliary optimization of $u(x)$ is a computationally inexpensive procedure and does not involve any FE based simulations since $u(x)$ is constructed using the predictions provided by a fast-to-evaluate GP model. The summary of the BO framework is illustrated in Fig. 5.

Among many possible BO based algorithms, in this paper, we use DPTBO (Torun and Swaminathan, 2019), which is a recently developed method that is suitable for high-dimensional sample spaces. In the context of material property characterization using the iFEM approach, the capability of handling high-dimensional problems enables managing complex material models with a high number of material constants, such as the Yeoh model. The reader is referred to (Torun and Swaminathan, 2019) for a more comprehensive overview of BO and the description of the DPTBO algorithm.

2.4. Evaluating uniqueness of the material properties

The output of the iFEM procedure is a single set of six material constants, namely the c_i values ($i = 1,2,3$) for the fibrous intima and the arterial wall, which are expected to be the best estimation. However, the uniqueness of the optimized solution is not guaranteed by just solving the optimization problem. Therefore, there is a necessity to check the uniqueness of the estimated material constants.

As explained in the previous section, the BO framework builds a GP model to replace the computationally expensive FE analysis with a fast-to-evaluate predictive method. It is therefore possible to use this GP model to rapidly evaluate the uniqueness of the estimated material constants, and obtain the range of parameters that would give the same error as the result of iFEM up to a pre-determined threshold.

Let e_{iFEM} be the final NMSE value obtained through iFEM, i.e. the global minimum of the optimization problem in (4). Our goal is to find N sets of material constant values, $x_{1:N}$, such that

$$f_{GP}(x_n) < e_{iFEM} + \sigma, \forall n = 1, \dots, N \quad (5)$$

where $f_{GP}(\cdot)$ is the GP predicted NMSE, σ is the user defined error threshold and x_n is the set of material constants. To obtain such x_n that would satisfy (5), we need to invert $f_{GP}(\cdot)$ as

$$\{x_n = f_{GP}^{-1}(y_n) \mid e_{iFEM} < y_n < e_{iFEM} + \sigma, \forall n = 1, \dots, N\} \quad (6)$$

Since $f_{GP}(\cdot)$ is likely to be a non-linear and non-monotonic function, its inverse, f_{GP}^{-1} , cannot be computed analytically. Therefore, we formulate the objective in (6) as a Bayesian problem and use a Markov Chain Monte Carlo (MCMC) method called as slice sampling (Neal, 2003) to estimate the distribution of solutions. More specifically, we want to sample from the material constants posterior given the final NMSE of iFEM, the GP model and the error threshold, i.e. $p(x \mid f_{GP}, e_{iFEM}, \sigma)$. Since this posterior is unknown, we use Bayes' Theorem, to represent it in terms of known quantities, given as

$$p(x \mid f_{GP}, e_{iFEM}, \sigma) \propto p(f_{GP} \mid x, e_{iFEM}, \sigma) p(x) \quad (7)$$

where $p(x)$ is the prior on material constants, taken as uniform distribution within the same bounds used for the iFEM. The likelihood in (7) can be written as

$$p(f_{GP} \mid x, e_{iFEM}, \sigma) = \mathcal{N}(f_{GP} \mid e_{iFEM}, \sigma^2)$$

where $\mathcal{N}(f_{GP} \mid e_{iFEM}, \sigma^2)$ represents a Gaussian random variable with a mean and standard deviation of e_{iFEM} and σ , respectively. The overall formulation then corresponds to using slice sampling to sample N new material constant values that are most likely to provide the same error with a complete iFEM procedure within the pre-specified error threshold of $e_{iFEM} < y_n < e_{iFEM} + \sigma$. The median of N different material constant values being close to the solution found by iFEM and their standard deviation being small enough implies that the material constant values found by iFEM are unique. We again would like to emphasize that the slice sampling method solely uses the GP model to obtain such material constant values. Since slice sampling, or any other MCMC method, needs to query the likelihood function numerous times, using FE analysis to calculate the likelihood in (8) would take significant computational resources and become impractical. By replacing the FE analysis with GP obtained after iFEM with BO, the proposed methodology can accurately evaluate the uniqueness of the solution in a rapid fashion.

3. Results

Multicomponent material properties of atherosclerotic carotid arteries were extracted from 13 cross sections of five human carotids using the developed iFEM approach. All cross sections had lipid pools, and three cross sections (# 5, 6 and 9) contained calcifications. The total plaque area ranged from 7 to 24 mm² with an average of 13 mm². The fibrous intima area ranged from 6 to 18 mm² with an average area of 10 mm², occupying 77% of the total plaque area, on average. The vessel wall area ranged from 19 to 34 mm².

The inflation experiments on all samples were successfully carried out with a stabilized minimal or no leakage. The MRI and ultrasound acquisitions were successfully performed and visually clear, high-resolution images were obtained for all samples. A representative atherosclerotic artery cross section (#8) is shown in Fig. 6, which demonstrates the corresponding MRI, ultrasound, FE model and iFEM outcome measurements. The presented axial displacements were obtained at the final pressure step of 120 mmHg. Qualitative visual assessment of the experimental displacements correctly indicated the effect of intraluminal pressurization locally: top portion displaced upwards and the bottom portion downwards (both regions with a maximum displacement amount of approximately 1 mm), whereas the central region showed minimal or no axial displacements. The magnitude of displacements at the luminal side was greater than abluminal regions as expected. Visual comparison of the color maps of experimental and computational demonstrated a good match. The NMSE value achieved by the iFEM approach for this cross section was 2%. The convergence was achieved in total of 88 FE model simulations following the sharp decrease in NMSE. The c_1 , c_2 and c_3 material constants obtained for the fibrous intima were 0.22, 0.44 and 375.23 kPa, and for the wall 24.63, -148.97 and 562.34 kPa, respectively.

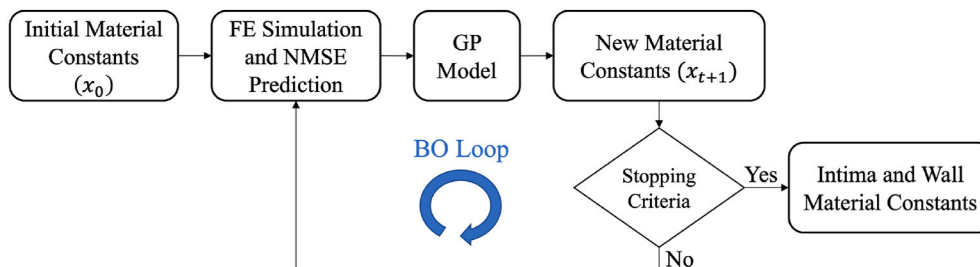


Fig. 5. A high-level summary of the Bayesian Optimization framework.

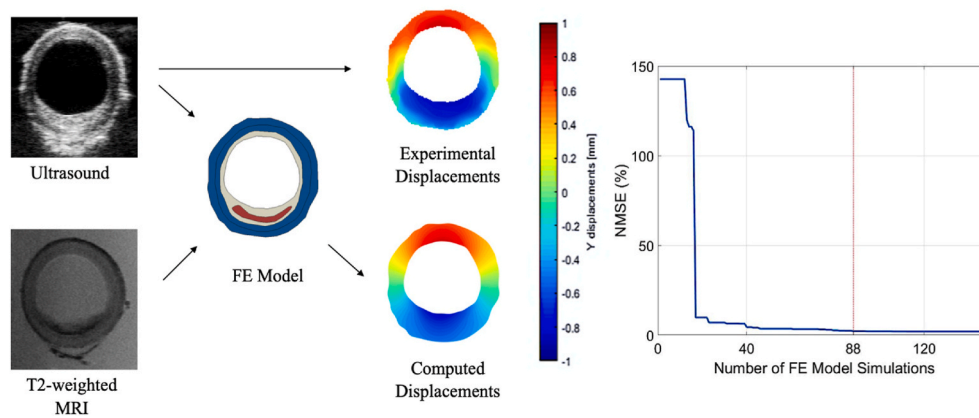


Fig. 6. The demonstration of the ultrasound and MR images, FE model, and the experimentally obtained and FE model predicted displacement maps of the representative cross section #8. The minimization scheme reached the optimized solution in 88 function evaluations, following the sharp decrease in the NMSE.

By using the developed iFEM approach, all cases achieved convergence well before the pre-set budget of 400 iterations, with an average of 133 iterations (approximately 7 hours by using Intel Xeon, 8 cores, 3.7 GHz CPU, 32 GB Ram). In overall, an average NMSE of $3.8\% \pm 2.1$ was successfully achieved for all cross sections. Sample and cross section specific computed Yeoh constants for fibrous intima and wall components are shown in Table I. The obtained material constants in Table I both for the intima and wall layers for all cross sections were observed to satisfy the stability criteria restriction (Bilgili, 2004) in (9) for the Yeoh model.

$$c_1 > 0, -\sqrt{3c_1c_3} < c_2 < \infty, c_3 > 0 \tag{9}$$

This criteria was also previously used by others (Lawlor et al., 2011), as negative c_2 were also observed while c_1 and c_3 parameters were in the positive range.

The combined final results for the fibrous intima and wall components of 13 cross sections are demonstrated in Fig. 7 (a). To check the uniqueness of the material constants given in Table I in a population based manner, the MCMC based methodology was used as described in Section II-G. The error threshold that determines uniqueness is chosen as $NMSE+5\%$ ($\sigma = 0.05$ in (6)) for each cross section. Then, the GPs that are trained for each of the 13 cross sections were used to predict $N = 500$ sets of additional material properties that would give an NMSE less than the original $NMSE + 5\%$, resulting in a total of 6500 sets of predicted material properties for all 13 cross sections combined. The boxplots of these predicted material properties are given in Fig. 7 (b), showing the median, 1st and 3rd quartiles of the predicted Yeoh model material constants for wall and fibrous intima. This is then compared to the iFEM-derived material constants obtained through 13 separate iFEM procedures given in Fig. 7(a).

Table 1

The estimated values of the Yeoh material constants for the fibrous intima and arterial wall by iFEM.

		Fibrous Intima (kPa)			Wall (kPa)			NMSE (%)
		c1	c2	c3	c1	c2	c3	
Sample 1	CS 1	20.60	-24.61	25.00	1.08	333.98	186.11	7
	CS 2	25.00	-19.34	242.50	0.59	-1.76	224.92	1
Sample 2	CS 3	27.80	-106.79	240.49	0.22	0.44	702.95	5
	CS 4	0.34	0.88	82.49	0.34	4.39	680.06	3
Sample 3	CS 5	19.14	-58.01	656.99	0.59	420.12	334.77	2
	CS 6	1.32	-14.94	210.64	8.16	450.88	280.95	3
	CS 7	3.03	3.52	71.87	22.56	-66.80	607.93	2
Sample 4	CS 8	0.22	0.44	375.23	24.63	-148.97	562.34	2
	CS 9	7.42	1.76	163.41	3.52	1.76	24.27	7
Sample 5	CS 10	1.81	21.97	278.75	0.34	0.88	363.70	4
	CS 11	22.56	-3.52	162.68	8.89	-3.52	189.04	7
	CS 12	4.01	14.06	568.38	27.44	-98.44	615.25	3
	CS 13	21.58	-21.09	747.07	2.05	232.03	20.61	4

For the fibrous intima, the medians for the iFEM-derived and the GP predicted c_1 , c_2 , and c_3 constants were 7.42, -3.52 and 240.49 kPa, and 11.42, -13.60, 235.44 kPa, respectively. For the wall, medians for the c_1 , c_2 , and c_3 constants were calculated as 2.05, 0.88, 334.77 kPa for the iFEM-derivations, and as 6.51, -0.72, 371.96 kPa for the GP-predicted solutions, respectively. Overall, the population based iFEM-derived (13 samples) and GP predicted (6500 samples) c_1 , c_2 , and c_3 values for both fibrous intima and wall demonstrated similar distributions (Fig. 7) and median values.

For an easier interpretation of the fibrous intima and wall material behaviour predicted in this study, Cauchy stress versus stretch ratio curves under uniaxial tensile stretch testing conditions were obtained using ABAQUS material evaluation functionality (Fig. 8). At 1.1, 1.2 and 1.4 stretch ratios, the Cauchy stress ranges for the fibrous intima were observed to be 0.35–14.74 kPa, 4.06–51.66 kPa, and 31.89–856.02 kPa, respectively (Fig. 8(a)). The average Cauchy stresses at these stretch ratios were 7.05, 22.54 and 331.13 kPa, respectively. For the wall, the Cauchy stress ranges at 1.1, 1.2 and 1.4 stretch ratios were 0.62–20.61 kPa, 5.73–138.24 kPa, and 39.57–1210.38 kPa, respectively (Fig. 8(b)). Average Cauchy stress calculations for these stretch ratios were 8.11, 47.04 and 602.87 kPa.

4. Discussion

In this study, we have demonstrated a pipeline to characterize component-wise material properties of atherosclerotic arteries from *ex-vivo* inflation tests. Our novel iFEM pipeline combines the physiological loading-mimicking inflation tests with high-resolution ultrasound based displacement estimation, high magnetic field MRI, FE modeling and a sample efficient optimization scheme. The iFEM pipeline was used for

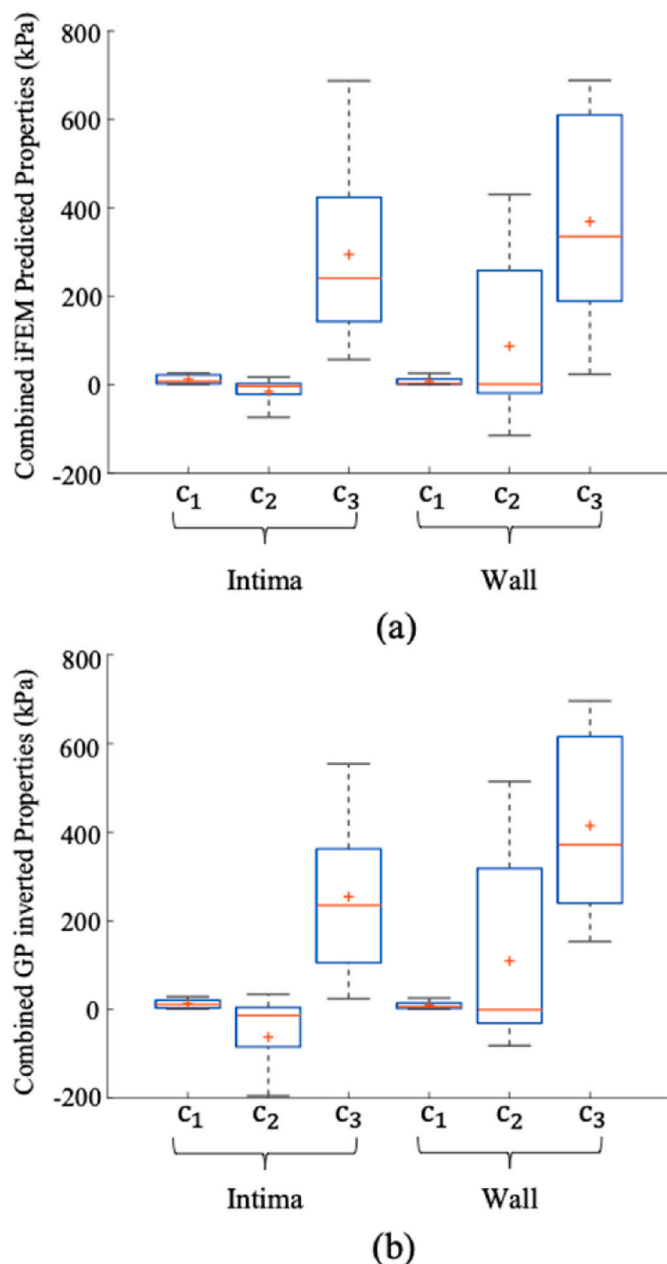


Fig. 7. The iFEM predicted results for 13 cross sections (a) and GP inverted model predictions (b) for checking a possible non-uniqueness existing in DPTBO based iFEM solutions.

the first time to extract the nonlinear properties of the fibrous intima and the vessel wall of atherosclerotic human carotids under physiological-like loading conditions. In all analyzed artery cross sections, convergence was achieved with a low error value ($<8\%$), which implies that 1.) a successful geometry registration between ultrasound and MRI was obtained, 2.) the non-linear tissue behaviour can be sufficiently captured with the Yeoh material model, and 3.) iFEM successfully predicted optimized material constants that represent tissue mechanical behavior. Furthermore, the good match between the iFEM-derived solutions and the MCMC based technique, explained in Section II.D, indicates population based uniqueness of the iFEM-derived solution sets.

Mechanical characterization of human atherosclerotic carotids plaques and arteries were also performed by some others previously, by using uniaxial tensile (Teng et al., 2009; Maher et al., 2009; Lawlor et al., 2011; Mulvihill and Walsh, 2013; Tenget al., 2014), (Davis et al., 2016), (O'Reilly et al., 2020), (Cunnaeet al., 2015), bi-axial tensile

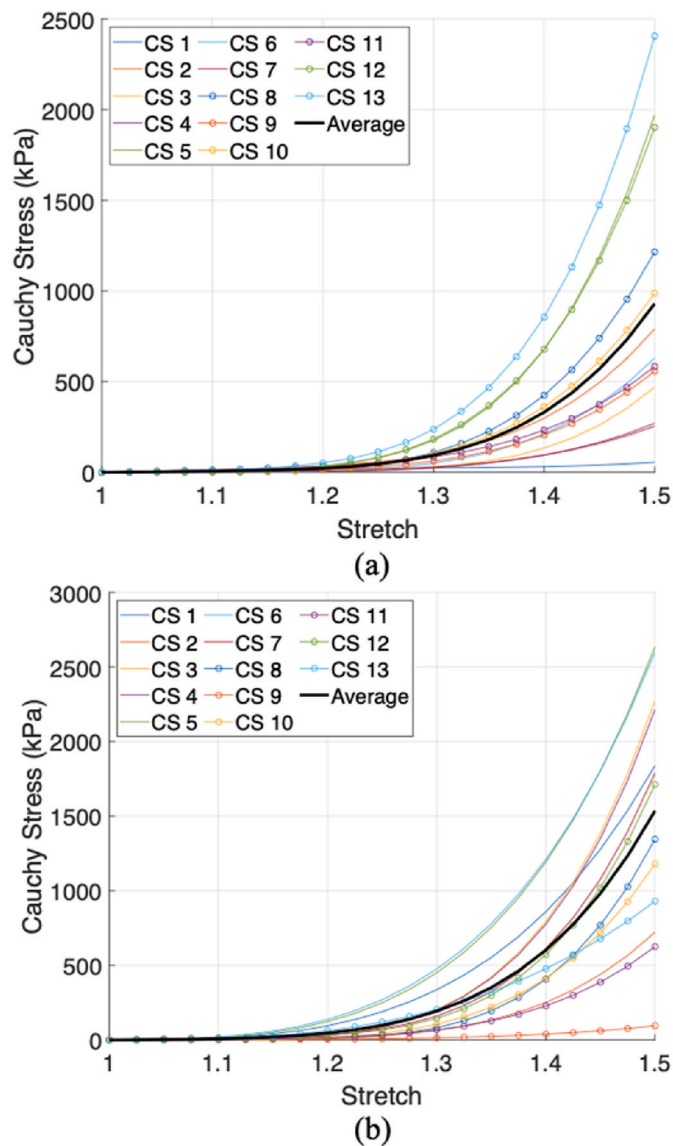


Fig. 8. Material behavior of the fibrous intima (a) and wall (b) layers based on the iFEM results under uniaxial tensile testing conditions of thought experiments.

(Kural et al., 2012), micro-indentation (Chaiet al., 2015; Barrett et al., 2009; Ebenstein et al., 2009), (Heiland et al., 2013) and compression tests (Maher et al., 2009), (O'Reilly et al., 2020). A major advancement we provide in our study is the component-based assessment of the material properties of atherosclerotic arteries whereas the above-mentioned studies were mainly limited to homogenous material characterization. Moreover, another important limitation of these studies were that the employed mechanical tests could not impose the multi-axial, physiological loading conditions. In contrast, our inflation tests closely mimic the *in-vivo* loading. Furthermore, intact arteries are used in inflation tests, as such tissue integrity is preserved in the test samples contrary to the samples used in the other mechanical tests. Although superior in these aspects, inflation tests come along with a challenge as the extraction of the material properties are not trivial and require advanced techniques, such as iFEM, presented in the current study. To overcome the possible immense computational cost of iFEM and minimize the number of the FEM simulations, we employed an advanced optimization scheme, the DPTBO algorithm. Commonly used optimization algorithms usually show slow convergence in CPU intensive black-box optimization problems (Torun and Swaminathan, 2019)

such as the iFEM. For instance, gradient-based methods require approximating the gradient by performing additional function queries, which can significantly degrade the convergence rate. When gradient-based methods are applied to non-convex problems, the optimization procedure needs to be restarted multiple times using different initial guesses to avoid a local minimum and reach the global minimum. Evolutionary based algorithms such as genetic algorithm and differential evolution, on the other hand, require a large number of iterations while using a large population size to avoid converging to a local minimum, which increases the number of function evaluations and can quickly become intractable. Contrarily, the BO-based methods such as DPTBO are quite favorable for problems such as the iFEM analysis due to its sample efficient, robust nature, also successfully demonstrated in the current study with fast convergence rates achieved.

The circumferential strain observed in all 13 of the cross sections from diastolic to systolic pressure levels (80–120 mmHg) ranged between 0.02 and 0.08 with an average (\pm SD) of 0.03 ± 0.01 . Segers et al. (Segers et al., 2004), investigated the in-vivo carotid artery circumferential vessel wall strains (distension) with respect to age, and they observed a strain range of approximately 0.03 and 0.08 for above 40 years. Hence, the strains computed in this work are observed to be in line with the in-vivo measurements. In the Cauchy stress versus the stretch ratio curves that were obtained in this work, non-linear behaviour was clearly observed for both the fibrous intima and the wall layers. It was also important to mention that the ranges and average Cauchy stress values observed for both the fibrous intima and wall were quite comparable. Due to the non-linear stiffening behaviour, the difference between the wall and fibrous intima was more clearly observed at 1.4 stretch ratio, in which the wall stress levels were slightly greater than the fibrous intima. Similar to our findings, Teng et al. (2014) have also reported comparable fibrous intima and media mechanical behaviour in their study where they have characterized component-wise human carotid endarterectomy samples with uni-axial tensile testing. However, they observed stiffer tissue properties in overall than our results, which may be attributed to difference of the samples. Since they have used endarterectomy samples in their study, the plaque tissue could be more at an advanced stage of the disease. Another relevant study was performed by Lawlor et al. (2011), in which the material behavior of human endarterectomy samples were predicted by Yeoh material models using uniaxial tensile test results. Although they have provided an overall characterization for the endarterectomy samples, they have categorized their samples as hard, mixed and soft. As the hard tissue group referred to highly calcified plaques, we compared our fibrous intima results to their mixed and soft group results. They demonstrated Cauchy stress ranges at 1.1, 1.2 and 1.4 stretch ratios between 1.4 and 38 kPa (average of 16.2 kPa), 10.8 to 80 (average of 32.5 kPa), and 105.8–193.9 kPa (average of 154.6 kPa) respectively for the soft; and 7.2–48.3 kPa (average of 19.1 kPa), 28.4–115.9 kPa (average of 66.9 kPa), and 431.4–593.2 kPa (average of 407.6 kPa) respectively for the mixed group. Their reported ranges were overall in line and slightly higher than the reported stress values in 1.1 and 1.2 stretch values for the fibrous intima. The Cauchy stress values in 1.4 stretch ratio provided in this work is in between both the soft and mixed ranges. Since they have provided overall homogeneous characterization for the endarterectomy samples, that could be a possible cause for the minimal difference in the reported values. Kural et al. (2012), performed bi-axial tensile testing on post-mortem atherosclerotic intact carotid arteries ($n = 4$) to obtain an overall estimation of the square shaped samples. Although the provided behaviours were not based on component-wise, the overall behaviour provides an important insight to compare with the wall layer properties predicted in this work. For 1.1 and 1.2 stretch ratio levels, they have observed Cauchy stress ranges of 13.4–24.5 kPa (an average of approximately 18.8 kPa), and 33.9–78.6 kPa (an average of approximately 57.2 kPa), respectively. The provided ranges are in accordance with the ranges for the wall component we observed. It is important to note that the mechanical behaviour of the cross section numbered 1 in

our work was observed to have quite low Cauchy stress values for fibrous intima. Similar low values were also observed by Lawlor et al. (2011).

There are some limitations associated with our study and the developed pipeline. (1) The Yeoh model is an isotropic material model, hence, cannot capture the anisotropic behavior of the wall and the fibrous intima. Yet, with the Yeoh models we reached low error values in iFEM. Implementation of anisotropic models in our iFEM pipeline warrants future research. (2) The experimental deformation data utilized in the iFEM framework was limited to the axial component of the displacement fields, obtained in the central region (covering the 50% width) of the cross sections. This choice is justified by the fact that the axial displacements in the central regions of the cross sections provide the most accurate ultrasound measurements, as the side regions undergo smaller axial displacements, leading to lower signal to noise ratio, and the lateral displacements estimated by cross-correlation technique was shown to have greater noise levels than the axial displacements (Akyildiz et al., 2016b). (3) The pre-stresses caused by the pre-loading of 10 mmHg to the reference geometry were not addressed in this study. Due to the nonlinear behavior of the arterial tissue, a significant effect from the 10 mmHg pressure compared to the zero pressurized arteries was not expected. (4) Our analyses were based on plain strain assumption in 2-D FE models, as the out-of-plane stretching was fixed in the longitudinal direction. (5) During the inflations testing, in case of minimal leakage, a small amount of continuous flow of PBS (maximum of 4.4 ml/min) with the syringe pump was used. This enabled stabilizing the intraluminal pressure. However, these flow levels are not expected to affect the quasi-static loading conditions, since the mean flow rate in healthy human common carotids were reported to be around 395 ± 79 mL per minute, and for the severely stenosed (higher than 70% stenosis) internal carotid arteries around 351 ± 109 mL per minute (Ackroyd et al., 1986). Some techniques have been proposed to quantify the residual stresses on atherosclerotic arteries (Delfino et al., 1997; Ohayon, 2007), (Ohayon et al., 2007), but the advancement on this issue is still limited due to the complex and heterogeneous structure of atherosclerotic plaque (Akyildiz et al., 2016b). Hence, they were not incorporated in the FE analysis. (7) The collection and handling of atherosclerotic intact human carotid artery is very challenging. Thus, only a limited number of carotid samples were studied. (8) In the current work, we focused on the mechanical characterization of the fibrous intima and wall components of atherosclerotic carotid arteries. Compared to these two, the other two tissue components, calcium and lipid, have distinct properties, the former being much stiffer (Gijssen et al., 2021) and the latter much more compliant (Loree et al., 1994), hence not included in the analysis. Yet, the established framework can be extended to also characterize these components. (9) 2-D approach was sufficient for this study as there was no longitudinal deformation in the arteries during the inflation test due to the applied pre-stretch. However, if needed, the entire iFEM framework can be further extended to 3-D, using the recent development of cross-correlation approach in 3-D (Fekkes, 2016; Hendriks et al., 2016).

Besides the great addition to our knowledge of component-wise material properties of human atherosclerotic carotid arteries, this study also presents a novel iFEM pipeline that has the potential for clinical translation. Although the impact of the associated relatively lower resolution requires further evaluation, by replacing the preclinical imaging systems used in the current study with their clinical counterparts, the developed pipeline can be used for in vivo characterization. This will provide a great advancement in plaque biomechanics field, as it will enable to overcome the big challenge of *in vivo*, plaque specific material characterization, crucial for the rupture risk assessment.

5. Conclusion

In this work, we presented a framework to characterize multicomponent material properties of atherosclerotic human carotid arteries. We obtained nonlinear properties of the fibrous intima and wall layers by

testing intact atherosclerotic carotids under physiological-like loading conditions *ex-vivo* and employing a machine-learning based optimization algorithm in a sample efficient manner. The trained optimization model provided the opportunity to check the uniqueness of the solution sets. The developed framework holds great potential for in-vivo application by using the clinical counterparts of the preclinical imaging techniques that were utilized in the current pipeline.

Author statement

Su Guvenir Torun: Methodology, Investigation, Software, Visualization, Writing-Original Draft, Hakki M. Torun: Software, Formal Analysis, Writing – Original Draft, Hendrik H.G. Hansen: Software, Writing – Review & Editing, Chris L. de Korte: Writing – Review & Editing, Antonius F.W. van der Steen: Project administration, Resources, Frank J.H. Gijzen: Supervision, Writing – Review & Editing, Ali C. Akyildiz: Conceptualization, Supervision, Funding acquisition, Resources, Writing – Review & Editing.

Declaration of competing interest

The authors declare that they have no known competing financial interests or personal relationships that could have appeared to influence the work reported in this paper.

Acknowledgment

This work was supported by the European Commission's Horizon 2020 research and innovation programme under the Marie Skłodowska-Curie grant agreement #749283. The authors thank Joost Haec, Suze-Anne Korteland, Michael Manten and Jaap Bongers for their support to the project.

References

- Ackroyd, N., Gill, R., Griffiths, K., Kossoff, G., Appleberg, M., 1986. "Quantitative common carotid artery blood flow: prediction of internal carotid artery stenosis. *J. Vasc. Surg.* 3 (6), 846–853. [https://doi.org/10.1016/0741-5214\(86\)90148-5](https://doi.org/10.1016/0741-5214(86)90148-5). Jun.
- Akyildiz, A.C., Speelman, L., Gijzen, F.J.H., 2014. "Mechanical properties of human atherosclerotic intima tissue. *J. Biomech.* 47 (4), 773–783. <https://doi.org/10.1016/j.jbiomech.2014.01.019>. Mar.
- Akyildiz, A.C., et al., 2011. "Effects of intima stiffness and plaque morphology on peak cap stress. *Biomed. Eng. Online* 10 (1), 25. <https://doi.org/10.1186/1475-925X-10-25>.
- Akyildiz, A.C., et al., 2016a. "The effects of plaque morphology and material properties on peak cap stress in human coronary arteries. *Comput. Methods Biomech. Biomed. Eng.* 19 (7), 771–779. <https://doi.org/10.1080/10255842.2015.1062091>. May.
- Akyildiz, A.C., et al., 2016b. "A framework for local mechanical characterization of atherosclerotic plaques: combination of ultrasound displacement imaging and inverse finite element analysis. *Ann. Biomed. Eng.* 44 (4), 968–979. <https://doi.org/10.1007/s10439-015-1410-8>. Apr.
- Akyildiz, A.C., et al., 2018. "Intima heterogeneity in stress assessment of atherosclerotic plaques. *Interface Focus* 8 (1), 20170008. <https://doi.org/10.1098/rsfs.2017.0008>. Feb.
- Barrett, S.R.H., Sutcliffe, M.P.F., Howarth, S., Li, Z., Gillard, J.H., 2009. "Experimental measurement of the mechanical properties of carotid atherothrombotic plaque fibrous cap. *J. Biomech.* 42 (11), 1650–1655. <https://doi.org/10.1016/j.jbiomech.2009.04.025>. Aug.
- Bilgili, E., 2004. "Restricting the hyperelastic models for elastomers based on some thermodynamical, mechanical, and empirical criteria. *J. Elastomers Plastics* 36 (2), 159–175. <https://doi.org/10.1177/0095244304042596>. Apr.
- Boekhoven, R.W., Peters, M.F.J., Rutten, M.C.M., van Sambeek, M.R., van de Vosse, F.N., Lopata, R.G.P., 2016. "Inflation and Bi-axial tensile testing of healthy porcine carotid arteries. *Ultrasound Med. Biol.* 42 (2), 574–585. <https://doi.org/10.1016/j.ultrasmedbio.2015.09.019>. Feb.
- Chai, C.-K., Speelman, L., Oomens, C.W.J., Baaijens, F.P.T., 2014. "Compressive mechanical properties of atherosclerotic plaques—indentation test to characterise the local anisotropic behaviour. *J. Biomech.* 47 (4), 784–792. <https://doi.org/10.1016/j.jbiomech.2014.01.018>. Mar.
- Chai, C.-K., et al., 2013. "Local axial compressive mechanical properties of human carotid atherosclerotic plaques—characterisation by indentation test and inverse finite element analysis. *J. Biomech.* 46 (10), 1759–1766. <https://doi.org/10.1016/j.jbiomech.2013.03.017>. Jun.
- Chai, C.-K., et al., 2015. "Local anisotropic mechanical properties of human carotid atherosclerotic plaques – characterisation by micro-indentation and inverse finite element analysis. *Journal of the Mechanical Behavior of Biomedical Materials* 43, 59–68. <https://doi.org/10.1016/j.jmbbm.2014.12.004>. Mar.
- Cheng, G.C., Loree, H.M., Kamm, R.D., Fishbein, M.C., Lee, R.T., 1993. "Distribution of circumferential stress in ruptured and stable atherosclerotic lesions. A structural analysis with histopathological correlation. *Circulation* 87 (4), 1179–1187. <https://doi.org/10.1161/01.CIR.87.4.1179>. Apr.
- Chun, Yuan, et al., 2002. "Identification of fibrous cap rupture with magnetic resonance imaging is highly associated with recent transient ischemic attack or stroke. *Circulation* 105 (2), 181–185. <https://doi.org/10.1161/hc0202.102121>. Jan.
- Cunnane, E.M., Mulvihill, J.J.E., Barrett, H.E., Hennessy, M.M., Kavanagh, E.G., Walsh, M.T., 2016. "Mechanical properties and composition of carotid and femoral atherosclerotic plaques: a comparative study. *J. Biomech.* 49 (15), 3697–3704. <https://doi.org/10.1016/j.jbiomech.2016.09.036>. Nov.
- Cunnane, E.M., et al., 2015. "Mechanical, biological and structural characterization of human atherosclerotic femoral plaque tissue. *Acta Biomater.* 11, 295–303. <https://doi.org/10.1016/j.actbio.2014.09.024>. Jan.
- Davis, L.A., Stewart, S.E., Carsten, C.G., Snyder, B.A., Sutton, M.A., Lessner, S.M., 2016. "Characterization of fracture behavior of human atherosclerotic fibrous caps using a miniature single edge notched tensile test. *Acta Biomater.* 43, 101–111. <https://doi.org/10.1016/j.actbio.2016.07.027>. Oct.
- Delfino, A., Stergiopoulos, N., Moore, J.E., Meister, J.-J., 1997. "Residual strain effects on the stress field in a thick wall finite element model of the human carotid bifurcation. *J. Biomech.* 30 (8), 777–786. [https://doi.org/10.1016/S0021-9290\(97\)00025-0](https://doi.org/10.1016/S0021-9290(97)00025-0). Aug.
- Ebenstein, D., Coughlin, D., Chapman, J., Pruitt, L., 2009. "Nanomechanical properties of calcification, fibrous tissue, and hematoma from atherosclerotic plaques. *J. Biomed. Mater. Res.* 91, 1028–1037. <https://doi.org/10.1002/jbm.a.32321>. Dec.
- Feigin, V.L., et al., 2014. "Global and regional burden of stroke during 1990–2010: findings from the global burden of disease study 2010," *the lancet*, vol. 383, no 9913, 245–255. [https://doi.org/10.1016/S0140-6736\(13\)61953-4](https://doi.org/10.1016/S0140-6736(13)61953-4). Jan.
- Fekkes, S., et al., 2016. "2-D versus 3-D cross-correlation-based radial and circumferential strain estimation using multiplane 2-D ultrafast ultrasound in a 3-D atherosclerotic carotid artery model. *IEEE Trans. Ultrason. Ferroelectrics Freq. Control* 63 (10), 1543–1553. <https://doi.org/10.1109/TUFFC.2016.2603189>. Oct.
- Gijzen, F.J.H., et al., 2021. "Morphometric and mechanical analyses of calcifications and fibrous plaque tissue in carotid arteries for plaque rupture risk assessment. *IEEE (Inst. Electron. Eng.) Trans. Biomed. Eng.* 68 (4), 1429–1438. <https://doi.org/10.1109/TBME.2020.3038038>. Apr.
- Hansen, H.H.G., Idzenga, T., de Korte, C.L., 2012. "Noninvasive vascular strain imaging: from methods to application. *Curr. Med. Imag. Rev.* 8, 37–45.
- Heiland, V.M., Forsell, C., Roy, J., Hedlin, U., Gasser, T.C., 2013. "Identification of carotid plaque tissue properties using an experimental-numerical approach. *Journal of the Mechanical Behavior of Biomedical Materials* 27, 226–238. <https://doi.org/10.1016/j.jmbbm.2013.05.001>. Nov.
- Hendriks, G.A.G.M., Holländer, B., Menssen, J., Milkowski, A., Hansen, H.H.G., de Korte, C.L., 2016. "Automated 3D ultrasound elastography of the breast: a phantom validation study. *Phys. Med. Biol.* 61 (7), 2665–2679. <https://doi.org/10.1088/0031-9155/61/7/2665>. Apr.
- Holzäpfel, G.A., Mulvihill, J.J., Cunnane, E.M., Walsh, M.T., 2014. "Computational approaches for analyzing the mechanics of atherosclerotic plaques: a review. *J. Biomech.* 47 (4), 859–869. <https://doi.org/10.1016/j.jbiomech.2014.01.011>. Mar.
- Horný, L., Adámek, T., Kulvajtová, M., 2017. "A comparison of age-related changes in axial prestretch in human carotid arteries and in human abdominal aorta. *Biomech. Model. Mechanobiol.* 16 (1), 375–383. <https://doi.org/10.1007/s10237-016-0797-y>. Feb.
- Klein, S., Staring, M., Murphy, K., Viergever, M.A., Pluim, J.P.W., 2010. "elastix: a toolbox for intensity-based medical image registration. *IEEE Trans. Med. Imag.* 29 (1), 196–205. <https://doi.org/10.1109/TMI.2009.2035616>. Jan.
- Kural, M.H., Cai, M., Tang, D., Gwyther, T., Zheng, J., Billiar, K.L., 2012. "Planar biaxial characterization of diseased human coronary and carotid arteries for computational modeling. *J. Biomech.* 45 (5), 790–798. <https://doi.org/10.1016/j.jbiomech.2011.11.019>. Mar.
- Lawlor, M.G., O'Donnell, M.R., O'Connell, B.M., Walsh, M.T., 2011. "Experimental determination of circumferential properties of fresh carotid artery plaques. *J. Biomech.* 44 (9), 1709–1715. <https://doi.org/10.1016/j.jbiomech.2011.03.033>. Jun.
- Leary, B.M., Taylor, M.G., 1966. "Alterations with age in the viscoelastic properties of human arterial walls. *Circ. Res.* 18 (3), 278–292. <https://doi.org/10.1161/01.RES.18.3.278>. Mar.
- Lopata, R.G.P., Nillesen, M.M., Hansen, H.H.G., Gerrits, I.H., Thijssen, J.M., de Korte, C.L., 2009. "Performance evaluation of methods for two-dimensional displacement and strain estimation using ultrasound radio frequency data. *Ultrasound Med. Biol.* 35 (5), 796–812. <https://doi.org/10.1016/j.ultrasmedbio.2008.11.002>. May.
- Loree, H.M., Kamm, R.D., Stringfellow, R.G., Lee, R.T., 1992. "Effects of fibrous cap thickness on peak circumferential stress in model atherosclerotic vessels. *Circ. Res.* 71 (4), 850–858. <https://doi.org/10.1161/01.RES.71.4.850>. Oct.
- Loree, H.M., Tobias, B.J., Gibson, L.J., Kamm, R.D., Small, D.M., Lee, R.T., 1994. "Mechanical properties of model atherosclerotic lesion lipid pools. *Arterioscler. Thromb.* 14 (2), 230–234. <https://doi.org/10.1161/01.ATV.14.2.230>. Feb.
- Maher, E., Creane, A., Sultan, S., Hynes, N., Lally, C., Kelly, D.J., 2009. "Tensile and compressive properties of fresh human carotid atherosclerotic plaques. *J. Biomech.* 42 (16), 2760–2767. <https://doi.org/10.1016/j.jbiomech.2009.07.032>. Dec.
- Maher, E., Creane, A., Sultan, S., Hynes, N., Lally, C., Kelly, D.J., 2011. "Inelasticity of human carotid atherosclerotic plaque. *Ann. Biomed. Eng.* 39 (9), 2445–2455. <https://doi.org/10.1007/s10439-011-0331-4>. Sep.

- Mozaffarian, D., et al., 2016. "Heart disease and stroke statistics—2016 update: a report from the American heart association. *Circulation* 133 (no. 4). <https://doi.org/10.1161/CIR.0000000000000350>. Jan.
- Mulvihill, J.J., Walsh, M.T., 2013. "On the mechanical behaviour of carotid artery plaques: the influence of curve-fitting experimental data on numerical model results. *Biomech. Model. Mechanobiol.* 12 (5), 975–985. <https://doi.org/10.1007/s10237-012-0457-9>. Oct.
- Neal, R.M., 2003. "Slice sampling. *Ann. Stat.* 31 (3), 705–767. <https://doi.org/10.1214/aos/1056562461>. Jun.
- Ohayon, J., et al., 2007. "Influence of residual stress/strain on the biomechanical stability of vulnerable coronary plaques: potential impact for evaluating the risk of plaque rupture. *Am. J. Physiol. Heart Circ. Physiol.* 293 (3), H1987–H1996. <https://doi.org/10.1152/ajpheart.00018.2007>. Sep.
- O'Reilly, B.L., Hynes, N., Sultan, S., McHugh, P.E., McGarry, J.P., 2020. "An experimental and computational investigation of the material behaviour of discrete homogenous iliofemoral and carotid atherosclerotic plaque constituents. *J. Biomech.* 106, 109801. <https://doi.org/10.1016/j.jbiomech.2020.109801>. Jun.
- Richardson, P., 1989. "Influence of plaque configuration and stress distribution on fissuring of coronary atherosclerotic plaques. *Lancet* 334 (8669), 941–944. [https://doi.org/10.1016/S0140-6736\(89\)90953-7](https://doi.org/10.1016/S0140-6736(89)90953-7). Oct.
- Rothwell, P., Warlow, C., 1999. "Prediction of benefit from carotid endarterectomy in individual patients: a risk-modelling study. *Lancet* 353 (9170), 2105–2110. [https://doi.org/10.1016/S0140-6736\(98\)11415-0](https://doi.org/10.1016/S0140-6736(98)11415-0). Jun.
- Sadat, U., Teng, Z., Young, V.E., Li, Z.Y., Gillard, J.H., 2011. "Utility of magnetic resonance imaging-based finite element analysis for the biomechanical stress analysis of hemorrhagic and non-hemorrhagic carotid plaques. *Circ. J.* 75 (4), 884–889. <https://doi.org/10.1253/circj.cj-10-0719>.
- Schaar, J.A., de Korte, C.L., Mastik, F., van der Steen, A.F.W., 2002. "Effect of temperature increase and freezing on intravascular elastography. *Ultrasonics* 40 (1), 879–881. [https://doi.org/10.1016/S0041-624X\(02\)00230-5](https://doi.org/10.1016/S0041-624X(02)00230-5). May.
- Segers, P., et al., 2004. "Functional analysis of the common carotid artery: relative distension differences over the vessel wall measured: in vivo. *J. Hypertens.* 22 (5), 973–981. May.
- Serfaty, J.-M., Chaabane, L., Tabib, A., Chevallier, J.-M., Briguët, A., Douek, P.C., 2001. "Atherosclerotic plaques: classification and characterization with T2-weighted high-spatial-resolution MR imaging—an in vitro study. *Radiology* 219 (2), 403–410. <https://doi.org/10.1148/radiology.219.2.r01ma15403>. May.
- Shamonin, D.P., Bron, E.E., Lelieveldt, B.P.F., Smits, M., Klein, S., Staring, M., 2014. "Fast parallel image registration on CPU and GPU for diagnostic classification of alzheimer's disease. *Front. Neuroinf.* 7 <https://doi.org/10.3389/fninf.2013.00050>.
- Shinnar, M., et al., 1999. "The diagnostic accuracy of ex vivo MRI for human atherosclerotic plaque characterization," *arteriosclerosis, Thrombosis, and Vascular Biology* 19 (11), 2756–2761. <https://doi.org/10.1161/01.ATV.19.11.2756>. Nov.
- Swaminathan, M., Torun, H.M., Yu, H., Hejase, J.A., Becker, W.D., 2020. "Demystifying machine learning for signal and power integrity problems in packaging. *IEEE Trans. Compon. Packag. Manuf. Technol.* 10 (8), 1276–1295. <https://doi.org/10.1109/TCPMT.2020.3011910>. Aug.
- Tavora, F., Cresswell, N., Li, L., Fowler, D., Burke, A., 2010. "Frequency of acute plaque ruptures and thin cap atheromas at sites of maximal stenosis. *Arq. Bras. Cardiol.* 94 (2), 153–159. <https://doi.org/10.1590/S0066-782X2010000200003>. Feb.
- Teng, Z., Tang, D., Zheng, J., Woodard, P.K., Hoffman, A.H., 2009. "An experimental study on the ultimate strength of the adventitia and media of human atherosclerotic carotid arteries in circumferential and axial directions. *J. Biomech.* 42 (15), 2535–2539. <https://doi.org/10.1016/j.jbiomech.2009.07.009>. Nov.
- Teng, Z., Sadat, U., Brown, A.J., Gillard, J.H., 2014. "Plaque hemorrhage in carotid artery disease: pathogenesis, clinical and biomechanical considerations. *J. Biomech.* 47 (4), 847–858. <https://doi.org/10.1016/j.jbiomech.2014.01.013>. Mar.
- Teng, Z., et al., 2014. "Material properties of components in human carotid atherosclerotic plaques: a uniaxial extension study. *Acta Biomater.* 10 (12), 5055–5063. <https://doi.org/10.1016/j.actbio.2014.09.001>. Dec.
- Torun, H.M., Swaminathan, M., 2019. "High-Dimensional global optimization method for high-frequency electronic design. *IEEE Trans. Microw. Theor. Tech.* 67 (6), 2128–2142. <https://doi.org/10.1109/TMTT.2019.2915298>. Jun.
- Wang, S., et al., 2019. "Bayesian inference-based estimation of normal aortic, aneurysmal and atherosclerotic tissue mechanical properties: from material testing, modeling and histology. *IEEE Trans. Biomed. Eng.* 66 (8), 2269–2278. <https://doi.org/10.1109/TBME.2018.2886681>. Aug.
- Yushkevich, P.A., et al., 2006. "User-guided 3D active contour segmentation of anatomical structures: significantly improved efficiency and reliability. *Neuroimage* 31 (3), 1116–1128. <https://doi.org/10.1016/j.neuroimage.2006.01.015>. Jul.